


 Cite this: *Nanoscale*, 2022, **14**, 9297

# Electrodeposited Sn–Cu@Sn dendrites for selective electrochemical CO<sub>2</sub> reduction to formic acid†

 Jinkyu Lim,<sup>a</sup> Angel T. Garcia-Esparza,<sup>c</sup> Jae Won Lee,<sup>a</sup> Gihun Kang,<sup>a</sup> Sangyong Shin,<sup>a</sup> Sun Seo Jeon<sup>a</sup> and Hyunjoo Lee<sup>a</sup>

Large-scale CO<sub>2</sub> electrolysis can be applied to store renewable energy in chemicals. Recent developments in gas diffusion electrodes now enable a commercially relevant current density. However, the low selectivity of the CO<sub>2</sub> reduction reaction (CO<sub>2</sub>RR) still hinders practical applications. The selectivity of the CO<sub>2</sub>RR highly depends on the electrocatalyst. Sn catalysts are considered promising cathode materials for the production of formic acid. The selectivity of Sn catalysts can be regulated by controlling their morphology or alloying them with secondary metals. Herein, we enhanced the selectivity of CO<sub>2</sub> reduction to formic acid by synthesizing Sn–Cu@Sn dendrites that have a core@shell architecture. The Sn–Cu@Sn dendrites were prepared by a scalable electro-deposition method. The electronic structure was modified to suppress a reaction pathway for CO production on the Sn surface. Notably, the Sn shell inhibited the cathodic corrosion of Cu during the CO<sub>2</sub>RR. On a gas diffusion electrode, the Sn–Cu@Sn dendrites exhibited 84.2% faraday efficiency to formic acid for 120 h with high stability.

 Received 22nd March 2022,  
Accepted 2nd June 2022

DOI: 10.1039/d2nr01563c

[rsc.li/nanoscale](https://rsc.li/nanoscale)

## Introduction

As a promising route for CO<sub>2</sub> capture and conversion, the electrochemical CO<sub>2</sub> reduction reaction (CO<sub>2</sub>RR) has attracted much attention.<sup>1,2</sup> CO<sub>2</sub> can be converted into useful chemical fuels by storing intermittent renewable power as stable chemical bonds.<sup>3</sup> A CO<sub>2</sub>RR with high current density is now feasible with a gas diffusion electrode (GDE) that delivers CO<sub>2</sub> gas to catalytically active sites at a solid–liquid–gas interface.<sup>4–6</sup> At least 16 different small molecules (*e.g.* carbon monoxide, formic acid, methane, ethylene, *etc.*) can be produced from the CO<sub>2</sub>RR, and the product distribution is mainly determined by the electrocatalytic materials.<sup>7,8</sup> Hence, catalysts highly selective toward high-value target products must be developed to upscale and deploy a practical CO<sub>2</sub> conversion technology.<sup>9</sup> The selectivity of the catalysts can be tuned by controlling the morphology of the catalyst, alloying it with other metals, or doping heteroatoms into the catalyst.<sup>1</sup> These approaches

change the adsorption energies or the orientations of the adsorbed reaction intermediates on the catalyst surface, which consequently alter the reaction pathways.<sup>10</sup>

Formic acid is a promising product that can be directly obtained from electrocatalytic CO<sub>2</sub>RR. The electrochemically produced formic acid can be used in direct fuel cells or utilized as a storage solution for renewable hydrogen.<sup>11</sup> Furthermore, the reaction pathway to formic acid is comparatively simple because it only requires a two *e*<sup>−</sup> transfer.<sup>12,13</sup> A selective and active electrocatalyst is needed to decrease the high activation energy (*i.e.*, the large CO<sub>2</sub>RR overpotential) and to suppress the competing hydrogen evolution reaction (HER) and CO production under the cathodic conditions.<sup>12</sup>

Sn has been identified as a Sabatier optimal metal for the CO<sub>2</sub>RR to formic acid<sup>14</sup> because it has a near-optimum binding strength to \*OCOH, which is generally known as a key reaction intermediate for formic acid.<sup>15</sup> Sn nanoparticles,<sup>16</sup> nanowires,<sup>17,18</sup> and mesoporous sheets<sup>19,20</sup> have all exhibited enhanced selectivity towards formic acid. Electrodeposited Sn electrodes with a dendritic shape or dense tips were also reported as selective CO<sub>2</sub>RR catalysts for formic acid.<sup>21,22</sup> Alloying with a secondary metal provides a straightforward way to modulate the electronic structure of Sn and thus the selectivity.<sup>23</sup> Cu is a particularly promising secondary metal for the CO<sub>2</sub>RR to formic acid when alloyed with Sn under certain compositions<sup>24</sup> as both Cu and Sn are earth-abundant metals and are easy to supply. Zheng *et al.* performed *in situ* X-ray absorp-

<sup>a</sup>Department of Chemical and Biomolecular Engineering, Korea Advanced Institute of Science and Technology, Daejeon 34141, South Korea. E-mail: [azhyun@kaist.ac.kr](mailto:azhyun@kaist.ac.kr)

<sup>b</sup>Linac Coherent Light Source, SLAC National Accelerator Laboratory, Menlo Park, California 94025, USA. E-mail: [jinkyu@slac.stanford.edu](mailto:jinkyu@slac.stanford.edu)

<sup>c</sup>Stanford Synchrotron Radiation Lightsource, SLAC National Accelerator Laboratory, Menlo Park, California 94025, USA

† Electronic supplementary information (ESI) available. See DOI: <https://doi.org/10.1039/d2nr01563c>

tion experiments and showed that the alloyed Sn with Cu was more electrophilic than pristine Sn even under CO<sub>2</sub> reducing conditions, which can suppress competing HER and CO production from the CO<sub>2</sub>RR.<sup>25</sup> However, some Sn–Cu alloy compositions were alternatively reported to be selective toward CO formation,<sup>26–29</sup> because the selectivity of Sn–Cu catalysts varies depending on the surface composition differences between the two metals.<sup>25,30</sup> A. Vasileff *et al.* showed a linear relationship between formic acid selectivity and Sn content in Sn–Cu alloy catalysts.<sup>30</sup> A Sn-rich surface is desired for selective formic acid formation.<sup>31</sup> However, shape control of the catalyst nanostructure for activity or selectivity optimization and their degradation mechanism during the reaction have been scarcely studied for Sn–Cu alloy catalysts.

Herein, Sn–Cu@Sn dendrites were prepared by a scalable electrodeposition method. A Sn–Cu alloyed core was obtained with a Sn-rich surface layer. The electrophilic Sn at the surface readily adsorbed the nucleophilic \*OCOH intermediate that can be further converted to formic acid. The dendritic shape made active sites more exposed and improved selectivity. Under the GDE cell configuration, the Sn–Cu@Sn dendrites showed enhanced activity and selectivity to formic acid when compared to Sn electrocatalysts. The stability of the alloyed electrocatalyst was also tested for operation on the GDE. The Sn shell suppressed the dissolution and re-electrodeposition of Cu during the CO<sub>2</sub>RR. A rapid degradation was observed once the shape of the catalysts was poorly controlled with exposure of the Cu core.

## Experimental section

### Cathode preparation with Sn–Cu@Sn dendrites

Sn–Cu@Sn dendrites were prepared by electrodeposition. To prepare a plating solution, solutions A and B were prepared separately. Solution A contained 0.5 M Na<sub>2</sub>SnO<sub>3</sub>·3H<sub>2</sub>O (95%, Sigma Aldrich) and 0.4 M NaOH (≥97.0%, Sigma Aldrich).<sup>21</sup> Solution B contained 0.17 M CuSO<sub>4</sub>·5H<sub>2</sub>O (≥98.0%, Sigma Aldrich), 1.2 M lactic acid (≥85%, Sigma Aldrich), and 1.5 M NaOH (≥97.0%, Sigma Aldrich). Then, 50 ml of solution A and 25 ml of solution B were mixed *via* magnetic stirring to prepare the plating solution. The working electrode was a carbon cloth (CC, CeTech) and the back side of the CC was coated with polytetrafluoroethylene (PTFE) with a loading of 0.3 mg<sub>PTFE</sub> cm<sup>−2</sup> to avoid contact with the plating solution and electrodeposition at the back. The CC was placed on a glass slide, and every edge was covered with an epoxy adhesive (Loctite® EA 9460™). The reference electrode was a Hg/HgO electrode (1 M NaOH, RE-61AP, ALS). The counter electrode was a graphite rod (WonATech). With a potentiostat (ZIVE BP2, WonATech) and a power booster (WonATech), a voltage of  $-4.0V_{\text{Hg}/\text{HgO}}$  was applied for 10 min for electrodeposition. The temperature of the plating solution was 25 °C. After the electrodeposition step, the working electrode was rinsed with deionized (DI) water and dried at 60 °C. The electrocatalysts on the electrode were collected with a disposable polypropylene

knife, washed with 0.5 M NaOH solution, washed further with DI water, and dried in a vacuum oven at 50 °C. A cathode was prepared as a gas diffusion electrode (GDE) by a N<sub>2</sub> spray method. The catalyst ink was prepared by dispersing 66 mg of catalysts into 5 ml of a mixture of isopropyl alcohol (>99.7%, Junsei) and ethyl alcohol (≤0.003% water, Sigma Aldrich) in a 3 : 1 volume ratio. A Nafion ionomer solution (69.9 μl; 10% aqueous solution, Sigma Aldrich) was added to the catalyst ink as a binder. The ink was N<sub>2</sub> sprayed on a carbon paper (Sigracet 39 BB) with a catalyst loading of 1.5 mg cm<sup>−2</sup> on a hot plate at 80 °C.

### Electrochemical CO<sub>2</sub> reduction

A customized GDE cell was used and its scheme is described in Fig. S1.†<sup>21</sup> The reference electrode was Ag/AgCl (3 M NaCl, BASi) and the anode was Ir oxide particles (99%, Alfa Aesar) deposited on a Ti diffusion layer (DL, Bekaert). An Ir oxide ink was prepared by dispersing 132 mg of Ir oxide in 5 ml of a mixture of isopropyl alcohol and ethyl alcohol in a 3 : 1 volume ratio. Then, 139.7 μl of the Nafion ionomer solution was added. After roll-pressing the Ti DL to a 180 μm thickness, the Ir oxide ink was sprayed on the pressed Ti DL with a catalyst loading of 3 mg cm<sup>−2</sup>. The geometric area of the electrode was 4 cm<sup>2</sup>. The electrolyte was CO<sub>2</sub>-saturated 1.0 M KHCO<sub>3(aq)</sub>. A Nafion 212 membrane was used. The flow rate of the CO<sub>2</sub> gas (99.999%) was 50 sccm. Each point on the *j*–*V* curves was collected after holding at a fixed current density for more than 30 min. The voltage was described in a reversible hydrogen electrode (RHE) using the following equation with 85% *i*R correction:

$$V_{\text{RHE}} = V_{\text{Ag}/\text{AgCl}} + V_{\text{Ag}/\text{AgCl}}^{\circ} + 0.0591 \times \text{pH} \quad (1)$$

For the electrochemical surface area (ECSA) estimation, double layer capacitance was measured by cyclic voltammetry (CV) cycles with scan rates of 10, 20, 40, 60, 80 and 100 mV s<sup>−1</sup>. A potentiostat (CHI 760E, CH Instruments) was used. A specific capacitance (*C<sub>s</sub>*) value of 0.033 mF cm<sup>−2</sup> was used for the ECSA calculation as follows:<sup>21</sup>

$$\text{ECSA} = C_{\text{DL}}/C_{\text{s}} \quad (2)$$

The commercial Sn nanoparticles (SnNP, Sigma Aldrich) were also tested as a benchmark. For the durability test, 250 ml of each electrolyte was circulated separately through the flow cell by two peristaltic pumps and galvanostatic CO<sub>2</sub> electrolysis was performed at  $-30 \text{ mA cm}^{-2}$  for 120 h. Gas products from the electrochemical reactions were analyzed *via* an online micro gas chromatograph (GC; Micro GC Fusion, Inficon) equipped with a Rt@-Molecular Sieve 5 Å and Rt@-Q-Bond columns (Inficon) with thermal conductivity detectors. The amount of formic acid produced in the electrolyte was quantified by a high-performance liquid chromatograph (HPLC; YL9100, Younglin) with a Hi-plex H column (Agilent) and a refractive index detector.

## Characterization

Transmission electron microscopy (TEM) images were obtained with a Cs-corrected transmission electron microscope (Titan cubed G2 60-300, FEI) with energy-dispersive X-ray spectroscopy (EDS). The Sn-Cu@Sn dendrites were also characterized by scanning electron microscopy (SEM; Magellan 400, FEI) and inductively coupled plasma mass spectrometry (ICP-MS; iCAP RQ, Thermo Fisher Scientific). The X-ray photoelectron spectroscope (XPS; K-alpha<sup>+</sup>, Thermo VG Scientific) used a monochromated Al K $\alpha$  X-ray source (12 kV, 3 mA). The binding energy was calibrated by locating the C 1s peak at 284.8 eV. The crystalline structure was analyzed using a powder X-ray diffractometer (XRD; SmartLab, Rigaku) with a Cu K $\alpha$  X-ray source. X-ray absorption near edge structure (XANES) spectra of the Sn K-edge were measured at the 10C beamline of the Pohang Light Source (PLS-II). The incident X-ray was monochromated by a Si(311) double-crystal. The spectra were collected in a transmission mode with high-precision ionization chamber detectors. The X-ray energy was calibrated with a reference Sn foil. The XANES data were processed with Athena software.

## Results and discussion

Sn-based dendrites were prepared by electrodeposition with a customized cell. Fig. 1(a) shows a low magnification SEM image of the morphology of the obtained dendrites. They were uniformly synthesized over the electrode area through electrodeposition in alkaline plating solutions. The dendrites were obtained on carbon cloth (CC) substrates by a single electrodeposition step with a plating solution that contained both Sn and Cu ions. The back side of the CC was coated with polytetrafluoroethylene (PTFE) to prevent electrodeposition at the back. The edges of the working electrode were blocked with an epoxy adhesive. Fig. S2<sup>†</sup> shows a photograph of the working electrode used for the electrodeposition. The geometric area of the exposed part was  $\sim 6.5$  cm<sup>2</sup>. The electrodeposition was performed for 10 min with a constant potential of  $-4.0V_{\text{Hg}/\text{HgO}}$ . The transient response of the current density is presented in Fig. S3<sup>†</sup>. The current density increased during the deposition process, likely due to the increasing surface area while forming the dendritic structure. After the electrodeposition, the powders were collected with a disposable polypropylene knife, washed, and finally dried.

The XRD diffractogram of the dendrites in Fig. 1(b) was ascribed to the diffraction peaks corresponding to both Sn<sub>1</sub>Cu<sub>1</sub> alloy and metallic Sn. A high angle annular dark field (HAADF) STEM image and its corresponding EDS mapping in Fig. 1(c) and (d) demonstrate the core-shell structure of the particles. Single elemental distributions are shown separately in Fig. 1(e) and (f). The elemental mapping result shows that the signals from Cu (red) were observed only at the core, while Sn was mostly detected at the surface. The microstructure of the surface is shown in the high resolution TEM (Fig. S4<sup>†</sup>) and SEM (Fig. S5<sup>†</sup>) images. The surface elemental composition was

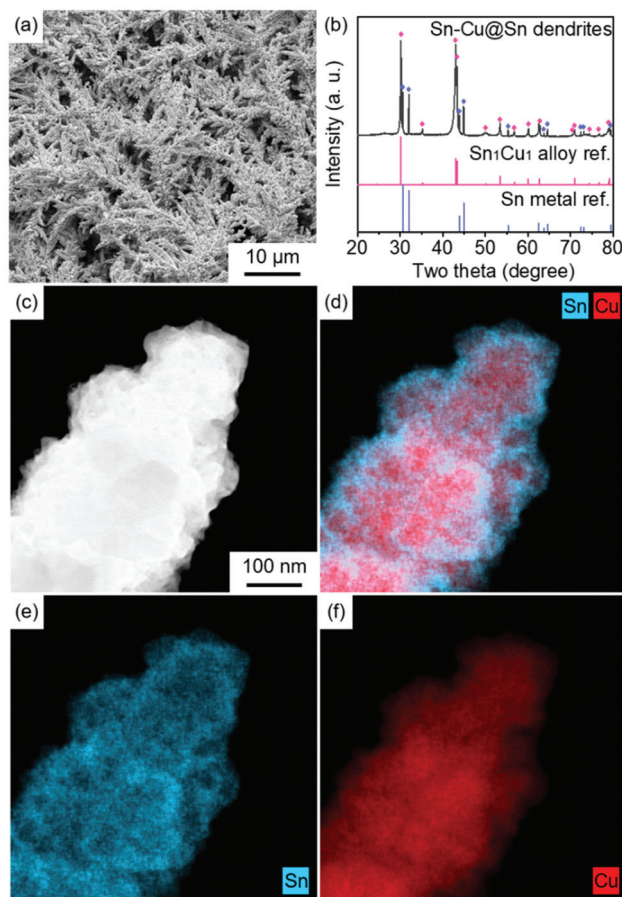


**Fig. 1** Characterization of electrodeposited Sn-Cu@Sn dendrites. (a) SEM image and (b) XRD pattern. Reference patterns for Sn<sub>1</sub>Cu<sub>1</sub> alloy (PDF#03-065-3434) and Sn metal (PDF#00-004-0673) are displayed together. (c) HAADF-STEM image and (d) the corresponding EDS mapping image of Sn-Cu@Sn dendrites. Blue and red dots on the EDS map represent the signals from Sn and Cu, respectively. Single element distributions of (e) Sn and (f) Cu shown separately.

estimated as Sn<sub>74</sub>Cu<sub>26</sub> via the XPS survey spectrum (Fig. S6<sup>†</sup>), while the overall composition of the dendrites was estimated to be Sn<sub>58</sub>Cu<sub>42</sub> via ICP-MS. The dendrites seem to have a core-shell structure consisting of a Sn-Cu alloy core with a Sn-rich shell, which is denoted as Sn-Cu@Sn below. When all the edges of the working electrode for electrodeposition were not sealed properly, a uniform core-shell structure was not obtained, as shown in Fig. S7<sup>†</sup>.

The electronic structure of the dendrites was investigated by X-ray spectroscopy techniques. For comparison, commercial Sn nanoparticles (SnNP, <150 nm) were also characterized. Fig. S8<sup>†</sup> shows the SEM images of the benchmark SnNP. The Sn 3d XPS spectra in Fig. 2(a) present two prominent peaks at 486.4 (3d<sub>5/2</sub>) and 494.8 eV (3d<sub>3/2</sub>), which are assigned to Sn<sup>2+</sup> in the Sn-Cu@Sn dendrites.<sup>32</sup> Metallic Sn<sup>0</sup> peaks were observed together at 484.9 (3d<sub>5/2</sub>) and 493.4 eV (3d<sub>3/2</sub>).<sup>32</sup> The atomic fraction of Sn<sup>2+</sup> on the Sn-Cu@Sn dendrites was 87.8% while the fraction of Sn<sup>0</sup> was 10.6% and the fraction for Sn<sup>4+</sup> was 1.6%. The Sn shell at the surface was moderately oxidized.

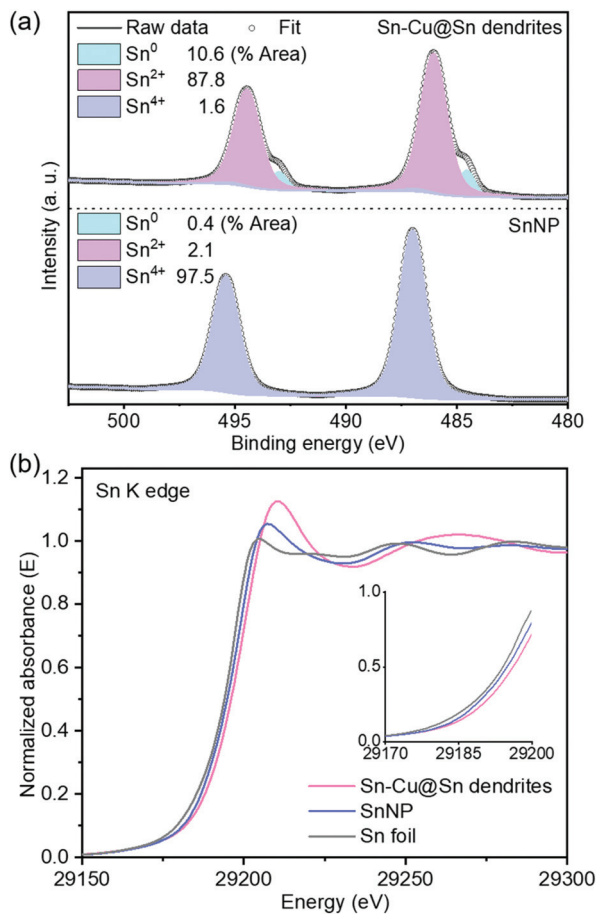


**Fig. 2** X-ray spectroscopy. (a) XPS spectra of the Sn  $3d_{3/2}$  and  $3d_{5/2}$  regions and (b) the Sn K-edge XANES spectra of the Sn-Cu@Sn dendrites and commercial SnNP catalysts. The inset image shows the pre-edge region of the spectra. Sn foil was used as a reference for XANES.

On the other hand, SnNP exhibited mostly Sn<sup>4+</sup> peaks at 487.0 ( $3d_{5/2}$ ) and 495.4 eV ( $3d_{3/2}$ ) with a fraction of 97.5% while the fraction of Sn<sup>0</sup> was 0.4% and the fraction of Sn<sup>2+</sup> was 2.1%, indicating that the surface of SnNP was heavily oxidized in the form of SnO<sub>2</sub>. It was previously shown that Sn<sup>2+</sup> species could enhance the selectivity of the CO<sub>2</sub>RR toward formic acid and stay stable even after long-term operation.<sup>33–35</sup>

Fig. 2(b) shows X-ray absorption near-edge structure (XANES) spectra at the Sn K-edge that provides the average bulk information of the particles. The number of unoccupied states can be qualitatively compared based on the main peak (*i.e.*, the white line intensity) from the XANES spectra. A higher white line intensity was observed for the Sn-Cu@Sn dendrites suggesting its oxidation state is higher than that of Sn foil or SnNP. Although the surface of the SnNP was more oxidized, the average oxidation state of SnNP was lower than Sn-Cu@Sn dendrites, implying that the SnNP has metallic a Sn core. The electron transfer from Sn to Cu enabled more electrophilic Sn in the Sn-Cu@Sn dendrites.

The CO<sub>2</sub>RR experiments were performed with a customized cell described in Fig. S1.† The electrodeposited Sn-Cu@Sn

dendrites were applied to the gas diffusion electrode (GDE) configuration, in which gaseous CO<sub>2</sub> can directly meet the catalyst surface. The facile mass transport can enhance current density and productivity.<sup>6,21</sup> The experimental assessments of the catalyst behavior of the GDE will facilitate the integrations of catalysts for an actual CO<sub>2</sub> electrolyzer.<sup>5,36</sup> After making a catalyst ink with isopropyl alcohol and ethanol solution, the ink was N<sub>2</sub>-sprayed onto a carbon paper (CP) with a catalyst loading of 1.5 mg cm<sup>-2</sup>. An Ag/AgCl electrode in 3 M NaCl was used as the reference electrode, an anode of Ir oxide NPs sprayed on a pressed Ti diffusion layer (DL) was used, and the catholyte and anolyte were separated by a Nafion 212 membrane. The SEM images of the bare Ti DL and Ir oxide nanoparticles coated on a Ti DL are presented in Fig. S9.†

The electrocatalytic properties of the Sn-Cu@Sn dendrites were characterized under conventional CO<sub>2</sub>RR conditions with a CO<sub>2</sub>-saturated bicarbonate buffer electrolyte at room temperature. Fig. 3(a) shows the  $j$ - $V$  curves of the Sn-Cu@Sn dendrites, the SnNP, and the bare CP substrate. All the points were obtained after 30 min of galvanostatic operation. The CP substrate was almost inert with a current density of less than  $-10$  mA cm<sup>-2</sup>, and the current came from the HER rather than the CO<sub>2</sub>RR. The Sn-Cu@Sn dendrites had significantly higher activity than the SnNP. To reach a current density of  $-30$  mA cm<sup>-2</sup>, the Sn-Cu@Sn dendrites required only  $-0.68V_{RHE}$  whereas the SnNP needed  $-0.92V_{RHE}$ . The electrochemical surface area (ECSA) of each catalyst was estimated from the double layer capacitance measurements as shown in Fig. S10.† With a given specific capacitance of 0.033 mF cm<sup>-2</sup> for Sn electrodes,<sup>21</sup> the Sn-Cu@Sn dendrites electrode had a 46% higher ECSA than the SnNP electrode (131.8 cm<sup>2</sup> and 90.3 cm<sup>2</sup>, respectively) due to the three-dimensional dendritic shape. When the  $j$ - $V$  curves were normalized by the ECSA, specific current densities were compared as shown in Fig. S11.† The Sn-Cu@Sn dendrites had higher specific activity. Facilitated activation of CO<sub>2</sub> to the \*OCOH intermediate on the electrophilic Sn surface can account for the higher intrinsic activity.<sup>25,30,31</sup> In addition, the dendritic structure at the electrode surface is advantageous to increase the local pH near the electrode, which facilitates the CO<sub>2</sub>RR by suppressing the competing HER.<sup>37–39</sup>

Fig. 3(b) and (c) show product distributions at various potentials with the Sn-Cu@Sn dendrites and the SnNP, respectively. When the applied potential was more positive than  $-0.4V_{RHE}$ , a competing side reaction, the hydrogen evolution reaction (HER) will dominate the Sn-Cu@Sn dendrites. Only a small amount of formic acid was accumulated in the catholyte while CO was barely observed. On the Sn-Cu@Sn dendrites, the Faraday efficiency to formic acid increased as a more negative potential was applied, and the highest selectivity of 84.2% was reached at  $-0.68V_{RHE}$ . Above this potential, CO formation, which is another competing reaction of CO<sub>2</sub>RR, increased gradually. For the SnNP, both Faraday efficiencies to CO and formic acid increased as a more negative potential was applied. The Faraday efficiency at  $-0.92V_{RHE}$  with a current density of  $-30$  mA cm<sup>-2</sup> was 54.8% on the SnNP benchmark

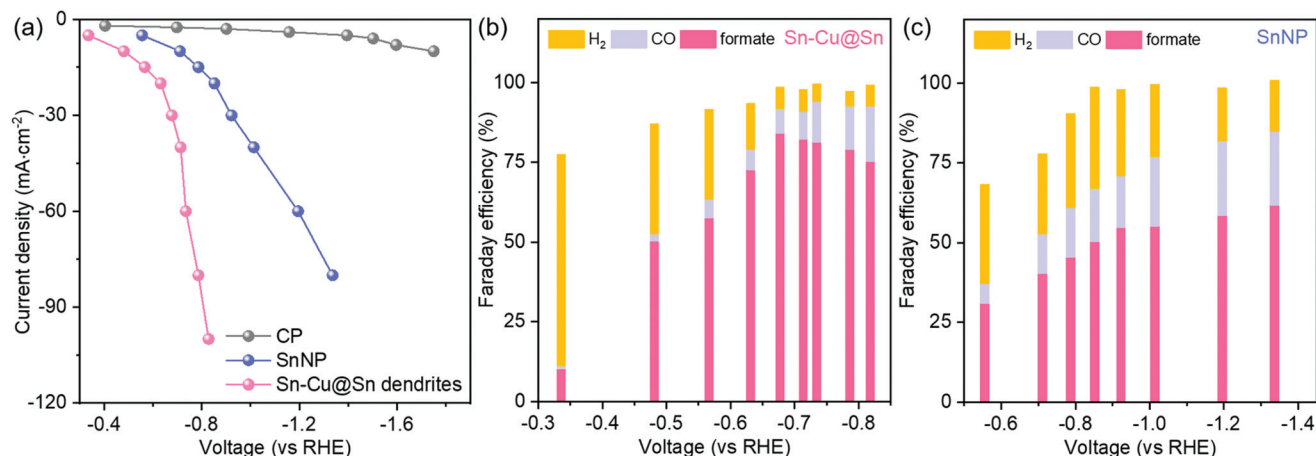


**Fig. 3** Electrochemical CO<sub>2</sub> reduction with Sn–Cu@Sn dendrites and SnNP catalysts on a GDE cathode. (a) *j*–*V* curves. Each point was obtained after a galvanostatic operation for 30 min. Measured Faraday efficiency on (b) Sn–Cu@Sn dendrites and (c) SnNP catalysts at different potentials. Measurement conditions: 4 cm<sup>2</sup> GDE, 1.5 mg cm<sup>−2</sup> catalyst loading, 1.0 M KHCO<sub>3(aq)</sub>, Ir oxide nanoparticles on pressed Ti DL as a counter electrode, Nafion 212 membrane, 25 °C.

catalyst. The Faraday efficiency increased slightly to 61.8% at a lower voltage of  $-1.34V_{\text{RHE}}$ . The Sn–Cu@Sn dendrites were more selective than the SnNP for formic acid production. Fig. S12<sup>†</sup> compares the selectivity ratios of formic acid over CO products at various potentials and catalysts. The CO<sub>2</sub>RR to formic acid was favored more than CO production on the Sn–Cu@Sn, especially in the low overpotential region. The high local pH of the nanostructured Sn electrodes suppresses the HER but can cause significant CO formation.<sup>21</sup> However, the CO<sub>2</sub>RR to CO was also suppressed by the Sn–Cu@Sn dendrites because of the rich Sn<sup>2+</sup> species.<sup>35</sup> The electrophilic Sn at the surface of the Sn–Cu@Sn dendrites was favorable for the adsorption of the \*OCOH intermediate, which is a key reaction intermediate for formic acid production.<sup>12,15</sup> The SnNP also had a rich oxidic Sn surface (Sn<sup>4+</sup>) due to the native oxide as confirmed in Fig. 2(a), but the CO<sub>2</sub>RR to formate was more favored on the Sn–Cu@Sn dendrites mainly with Sn<sup>2+</sup> species at the surface that are known to give higher activation energy barriers to the competing reactions.<sup>35</sup> The partial current densities toward each product at various potentials are compared in Fig. S13.<sup>†</sup> The partial current density to formic acid reached  $-75.4 \text{ mA cm}^{-2}$  at  $-0.82V_{\text{RHE}}$  on the Sn–Cu@Sn dendrites while the SnNP had only  $-10.1 \text{ mA cm}^{-2}$  at  $-0.85V_{\text{RHE}}$ . In Table S1,<sup>†</sup> the CO<sub>2</sub>RR parameters of the Sn–Cu@Sn dendrites for formic acid production were compared with those of the state of the art catalysts in the literature.

The durability of the Sn–Cu@Sn dendrites was tested by performing CO<sub>2</sub> electrolysis on the GDE configuration. Fig. 4 shows the chronopotentiometry result at a current density of  $-30 \text{ mA cm}^{-2}$  for 120 h. The voltage was stable at  $\sim -0.68V_{\text{RHE}}$ , and there was only a minor decrease in the Faraday efficiency to formic acid from 82% to 77%. Fig. S14<sup>†</sup> shows the SEM images and XPS spectrum for the Sn–Cu@Sn dendrites after the durability test. Even after operation for 120 h, the dendritic morphology was barely changed. The atomic fraction of Sn<sup>2+</sup>

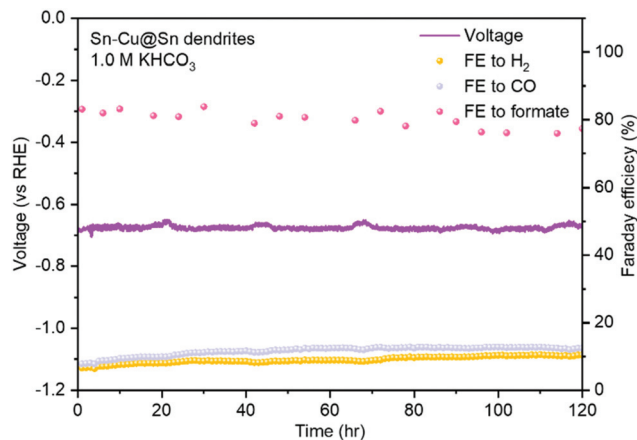


**Fig. 4** Prolonged CO<sub>2</sub>RR using Sn–Cu@Sn dendrites in a customized GDE electrolysis cell for 120 h. Measurement conditions: 4 cm<sup>2</sup> GDE, 1.0 M KHCO<sub>3(aq)</sub>, Ir oxide nanoparticles on pressed Ti DL as a counter electrode, Nafion 212 membrane, 25 °C.

species on the surface was 86.6% after the reaction, consistent with that at the beginning, while the fraction of Sn<sup>4+</sup> slightly increased to 5.2%.

However, a poorly shape-controlled catalyst was not stable for the CO<sub>2</sub>RR. The electrodeposited particles shown in Fig. S7<sup>†</sup> were tested for the CO<sub>2</sub>RR using the GDE configuration and the results are shown in Fig. S15(a).<sup>†</sup> Although the initial performance was similar, rapid degradation was observed in the product distribution. Faraday efficiency to parasitic HER increased from  $\sim 5\%$  to  $\sim 25\%$  during the 80 h test, while the Faraday efficiency to formic acid decreased to 48% after the first 16 h and then to 36% at the end of the 80 h test. Fig. S15(b) and (c)<sup>†</sup> show an SEM image and the EDS mapping results of the catalysts after the durability test. The

dendritic shape collapsed and Cu nanowhiskers were observed. The Cu surface exposed to the electrolyte underwent cathodic corrosion and then re-deposited on the electrode.<sup>40</sup> For stable and selective CO<sub>2</sub>RR to formic acid, the Sn shell at the surface was required on the Sn–Cu alloy, which can prevent the cathodic corrosion of Cu.

## Conclusions

Scalable and selective catalysts applicable to GDE should be developed for practical deployment of the CO<sub>2</sub>RR to formic acid. The Sn–Cu@Sn dendrites were prepared by a facile electrodeposition method in a single step. The dendrites are composed of a Sn–Cu alloy at the core and a Sn-rich shell at the surface. When the Sn–Cu@Sn dendrites were applied to a GDE, the activity and selectivity to formic acid were significantly enhanced compared with commercial SnNP. For the same current density of  $-30 \text{ mA cm}^{-2}$ , the Faraday efficiency to formic acid reached 84.2% at  $-0.68V_{\text{RHE}}$  for the Sn–Cu@Sn dendrites, whereas Faraday efficiency was 54.8% at  $-0.92V_{\text{RHE}}$  for SnNP. The electrophilic Sn surface may enable favorable adsorption of the nucleophile \*OCOH intermediate that would be further converted to formic acid. The durability was checked by performing the CO<sub>2</sub>RR on the GDE for 120 h at  $-30 \text{ mA cm}^{-2}$ . Faraday efficiency, product distribution, and voltage were barely changed. The Sn shell enabled stable long-term operation by suppressing the cathodic corrosion of Cu and its subsequent re-deposition on the cathode. This work can contribute to the design of electrocatalysts for selective formic acid production through large-scale CO<sub>2</sub>RR.

## Author contributions

J. Lim conceived the project, conducted most experiments, and wrote the manuscript. A. T. Garcia-Esparza contributed to data analysis and edited the manuscript. J. Lim, J. W. Lee, and G. Kang performed the electrochemical analysis. J. Lim, J. W. Lee, and S. Shin conducted the characterization experiments. J. Lim, J. W. Lee, and S. S. Jeon prepared the electrocatalysts. H. Lee supervised the project, provided the resources, and finalized the manuscript.

## Conflicts of interest

There are no conflicts to declare.

## Acknowledgements

This work was financially supported by the National Research Foundation of Korea (NRF-2016R1A5A1009592, 2017M3D1A1040692, and 2019M3D1A1079306).

## Notes and references

- 1 Y. Y. Birdja, E. Pérez-Gallent, M. C. Figueiredo, A. J. Göttle, F. Calle-Vallejo and M. T. M. Koper, *Nat. Energy*, 2019, **4**, 732–745.
- 2 H. S. Whang, J. Lim, M. S. Choi, J. Lee and H. Lee, *BMC Chem. Eng.*, 2019, **1**, 9.
- 3 P. De Luna, C. Hahn, D. Higgins, S. A. Jaffer, T. F. Jaramillo and E. H. Sargent, *Science*, 2019, **364**, eaav3506.
- 4 D. Higgins, C. Hahn, C. Xiang, T. F. Jaramillo and A. Z. Weber, *ACS Energy Lett.*, 2019, **4**, 317–324.
- 5 T. Burdyny and W. A. Smith, *Energy Environ. Sci.*, 2019, **12**, 1442–1453.
- 6 J. Lee, J. Lim, C.-W. Roh, H. S. Whang and H. Lee, *J. CO<sub>2</sub> Util.*, 2019, **31**, 244–250.
- 7 S. Nitopi, E. Bertheussen, S. B. Scott, X. Liu, A. K. Engstfeld, S. Horch, B. Seger, I. E. L. Stephens, K. Chan, C. Hahn, J. K. Nørskov, T. F. Jaramillo and I. Chorkendorff, *Chem. Rev.*, 2019, **119**, 7610–7672.
- 8 K. P. Kuhl, E. R. Cave, D. N. Abram and T. F. Jaramillo, *Energy Environ. Sci.*, 2012, **5**, 7050–7059.
- 9 O. S. Bushuyev, P. De Luna, C. T. Dinh, L. Tao, G. Saur, J. van de Lagemaat, S. O. Kelley and E. H. Sargent, *Joule*, 2018, **2**, 825–832.
- 10 M. B. Ross, P. De Luna, Y. Li, C.-T. Dinh, D. Kim, P. Yang and E. H. Sargent, *Nat. Catal.*, 2019, **2**, 648–658.
- 11 S. Enthaler, J. von Langermann and T. Schmidt, *Energy Environ. Sci.*, 2010, **3**, 1207–1217.
- 12 C. W. Lee, N. H. Cho, K. D. Yang and K. T. Nam, *ChemElectroChem*, 2017, **4**, 2130–2136.
- 13 F. Proietto, A. Galia and O. Scialdone, *ChemElectroChem*, 2019, **6**, 162–172.
- 14 Q. Li, X. Rao, J. Sheng, J. Xu, J. Yi, Y. Liu and J. Zhang, *J. CO<sub>2</sub> Util.*, 2018, **27**, 48–59.
- 15 J. T. Feaster, C. Shi, E. R. Cave, T. Hatsukade, D. N. Abram, K. P. Kuhl, C. Hahn, J. K. Nørskov and T. F. Jaramillo, *ACS Catal.*, 2017, **7**, 4822–4827.
- 16 J. Gu, F. Héroguel, J. Luterbacher and X. Hu, *Angew. Chem., Int. Ed.*, 2018, **57**, 2943–2947.
- 17 B. Kumar, V. Atla, J. P. Brian, S. Kumari, T. Q. Nguyen, M. Sunkara and J. M. Spurgeon, *Angew. Chem., Int. Ed.*, 2017, **56**, 3645–3649.
- 18 S. Liu, J. Xiao, X. F. Lu, J. Wang, X. Wang and X. W. Lou, *Angew. Chem., Int. Ed.*, 2019, **58**, 8499–8503.
- 19 F. Wei, T. Wang, X. Jiang, Y. Ai, A. Cui, J. Cui, J. Fu, J. Cheng, L. Lei, Y. Hou and S. Liu, *Adv. Funct. Mater.*, 2020, **30**, 2002092.
- 20 F. Li, L. Chen, G. P. Knowles, D. R. MacFarlane and J. Zhang, *Angew. Chem., Int. Ed.*, 2017, **56**, 505–509.
- 21 J. Lim, P. W. Kang, S. S. Jeon and H. Lee, *J. Mater. Chem. A*, 2020, **8**, 9032–9038.
- 22 D. H. Won, C. H. Choi, J. Chung, M. W. Chung, E.-H. Kim and S. I. Woo, *ChemSusChem*, 2015, **8**, 3092–3098.
- 23 X. Zhang, F. Li, Y. Zhang, A. M. Bond and J. Zhang, *J. Mater. Chem. A*, 2018, **6**, 7851–7858.

- 24 M. Morimoto, Y. Takatsuji, S. Iikubo, S. Kawano, T. Sakakura and T. Haruyama, *J. Phys. Chem. C*, 2019, **123**, 3004–3010.
- 25 X. Zheng, Y. Ji, J. Tang, J. Wang, B. Liu, H.-G. Steinrück, K. Lim, Y. Li, M. F. Toney, K. Chan and Y. Cui, *Nat. Catal.*, 2019, **2**, 55–61.
- 26 J. Zeng, K. Bejtka, W. Ju, M. Castellino, A. Chiodoni, A. Sacco, M. A. Farkhondehfar, S. Hernández, D. Rentsch, C. Battaglia and C. F. Pirri, *Appl. Catal., B*, 2018, **236**, 475–482.
- 27 Y. Zhao, C. Wang and G. G. Wallace, *J. Mater. Chem. A*, 2016, **4**, 10710–10718.
- 28 W. J. Dong, J. W. Lim, D. M. Hong, J. Y. Park, W. S. Cho, S. Baek, C. J. Yoo, W. Kim and J.-L. Lee, *ACS Appl. Energy Mater.*, 2020, **3**, 10568–10577.
- 29 S. Sarfraz, A. T. Garcia-Esparza, A. Jedidi, L. Cavallo and K. Takanebe, *ACS Catal.*, 2016, **6**, 2842–2851.
- 30 A. Vasileff, X. Zhi, C. Xu, L. Ge, Y. Jiao, Y. Zheng and S.-Z. Qiao, *ACS Catal.*, 2019, **9**, 9411–9417.
- 31 Q. Li, J. Fu, W. Zhu, Z. Chen, B. Shen, L. Wu, Z. Xi, T. Wang, G. Lu, J.-J. Zhu and S. Sun, *J. Am. Chem. Soc.*, 2017, **139**, 4290–4293.
- 32 J. Wu, X. Bai, Z. Ren, S. Du, Z. Song, L. Zhao, B. Liu, G. Wang and H. Fu, *Nano Res.*, 2021, **14**, 1053–1060.
- 33 Y.-W. Choi, F. Scholten, I. Sinev and B. Roldan Cuenya, *J. Am. Chem. Soc.*, 2019, **141**, 5261–5266.
- 34 R. Zhang, W. Lv and L. Lei, *Appl. Surf. Sci.*, 2015, **356**, 24–29.
- 35 X. An, S. Li, A. Yoshida, Z. Wang, X. Hao, A. Abudula and G. Guan, *ACS Sustainable Chem. Eng.*, 2019, **7**, 9360–9368.
- 36 M. F. Lagadec and A. Grimaud, *Nat. Mater.*, 2020, **19**, 1140–1150.
- 37 F. Scholten, I. Sinev, M. Bernal and B. Roldan Cuenya, *ACS Catal.*, 2019, **9**, 5496–5502.
- 38 A. S. Hall, Y. Yoon, A. Wuttig and Y. Surendranath, *J. Am. Chem. Soc.*, 2015, **137**, 14834–14837.
- 39 J. Lim, H. Lim, B. Kim, S. M. Kim, J.-B. Lee, K. R. Cho, H. Choi, S. Sultan, W. Choi, W. Kim and Y. Kwon, *Electrochim. Acta*, 2021, 139190.
- 40 P. De Luna, R. Quintero-Bermudez, C.-T. Dinh, M. B. Ross, O. S. Bushuyev, P. Todorović, T. Regier, S. O. Kelley, P. Yang and E. H. Sargent, *Nat. Catal.*, 2018, **1**, 103–110.